Journal of Microscopy

Journal of Microscopy, Vol. 278, Issue 2 2020, pp. 59–75
Received 19 February 2019; accepted 4 March 2020

doi: 10.1111/jmi.12887

Optimising adjacent membrane segmentation and parameterisation in multicellular aggregates by piecewise active contours

J. JARA-WILDE*,†, I. CASTRO†,‡, C.G. LEMUS†,‡, K. PALMA†,‡, F. VALDÉS†,§, V. CASTAÑEDA‖, N. HITSCHFELD*, M.L. CONCHA†,‡,# & S. HÄRTEL†,‡,**

*Departamento de Ciencias de la Computación, FCFM, Universidad de Chile, Santiago, Chile

†Biomedical Neuroscience Institute, Santiago, Chile

‡Programa de Anatomía y Biología del Desarrollo, ICBM, FMed, Universidad de Chile, Santiago, Chile

§Escuela de Tecnología Médica, FMed, Universidad de Chile, Santiago, Chile

‖Departamento de Tecnología Médica, FMed, Universidad de Chile, Santiago, Chile

#Geroscience Center for Brain Health and Metabolism (GERO), Santiago, Chile

**Centro de Informática Médica y Telemedicina, FMed, Universidad de Chile, Santiago, Chile

Key words. Active contours, adjacent membranes, cell adhesion, fluorescence microscopy, image processing, segmentation.

Summary

In fluorescence microscopy imaging, the segmentation of adjacent cell membranes within cell aggregates, multicellular samples, tissue, organs, or whole organisms remains a challenging task. The lipid bilayer is a very thin membrane when compared to the wavelength of photons in the visual spectra. Fluorescent molecules or proteins used for labelling membranes provide a limited signal intensity, and light scattering in combination with sample dynamics during *in vivo* imaging lead to poor or ambivalent signal patterns that hinder precise localisation of the membrane sheets. In the proximity of cells, membranes approach and distance each other. Here, the presence of membrane protrusions such as blebs; filopodia and lamellipodia; microvilli; or membrane vesicle trafficking, lead to a plurality of signal patterns, and the accurate localisation of two adjacent membranes becomes difficult.

Several computational methods for membrane segmentation have been introduced. However, few of them specifically consider the accurate detection of adjacent membranes. In this article we present ALPACA (ALgorithm for Piecewise Adjacent Contour Adjustment), a novel method based on 2D piecewise parametric active contours that allows: (i) a definition of proximity for adjacent contours, (ii) a precise detection of adjacent, nonadjacent, and overlapping contour sections, (iii) the definition of a polyline for an optimised shared contour within adjacent sections and (iv) a solution for connecting adjacent and nonadjacent sections under the constraint of preserving the inherent cell morphology.

We show that ALPACA leads to a precise quantification of adjacent and nonadjacent membrane zones in regular hexagons and live image sequences of cells of the parapineal organ during zebrafish embryo development. The algorithm detects and corrects adjacent, nonadjacent, and overlapping contour sections within a selected adjacency distance d, calculates shared contour sections for neighbouring cells with minimum alterations of the contour characteristics, and presents piecewise active contour solutions, preserving the contour shape and the overall cell morphology. ALPACA quantifies adjacent contours and can improve the meshing of 3D surfaces, the determination of forces, or tracking of contours in combination with previously published algorithms. We discuss pitfalls, strengths, and limits of our approach, and present a guideline to take the best decision for varying experimental conditions for *in vivo* microscopy.

Introduction

Perception and quantitative understanding of the form of living cells and tissue contribute substantially to our knowledge in biomedicine. Examples from studies related to morphogenesis, wound healing, or diseases are manifold and have motivated the development of image processing techniques and software packages in 2D and 3D (Mosaliganti *et al.*, 2012; Brodland *et al.*, 2014; Veldhuis *et al.*, 2017). The morphology of single cells and their organisation with respect to adjacent

Correspondence to: S. Härtel, Universidad de Chile, Instituto de Ciencias Biomédicas, Biomedical Neuroscience Institute, 1027 Av. Independencia, Independencia 8380453, Santiago, Chile. Tel: +56 2 29786366. E-mail: shartel@med.uchile.cl

cells are relevant for the mediation of cell–cell communication through biochemical signals (proteins, lipids, ions or gases), or mechanical stimuli through direct, physical contact (Veldhuis *et al.*, 2017). For the quantification of cell morphology and its relation with the surrounding context (like other cells and/or extracellular matrix), the cell contours have to be identified and localised correctly.

Cells can exert or respond to forces, and physical contact can stimulate or inhibit the formation of cell protrusions or migration (Richardson *et al.*, 2016; Reig *et al.*, 2017). Physical contact between cell membranes has been quantified by the adjacency of neighbouring membrane contours from images of different experimental conditions that often involve time-lapse series. Despite recent advances (Mosaliganti *et al.*, 2012; Brodland *et al.*, 2014; Stegmaier *et al.*, 2016; Dufour *et al.*, 2017; Farrell *et al.*, 2017; Veldhuis *et al.*, 2017), the segmentation of adjacent membranes in cell aggregates, multicellular samples, tissue, organs, or whole organisms from fluorescence microscopy images remains a challenging task. For *in vivo* imaging of cells within whole organisms, the quantification of adjacent and nonadjacent membrane sections under the conservation of the morphology of individual cell contours has not been solved satisfactorily so far.

Fast optical microscopy is the method of choice when it comes to *in vivo* observation and quantification of cellular dynamics, migration, tissue formation, or organisation of whole organisms. The development of fast confocal microscopy techniques such as spinning disc or light sheet, in combination with fluorescent markers that can be encoded genetically, expressed *in vivo* and targeted to cell nuclei, organelles, membranes, or further constituents, contribute to increasing spatial–temporal resolutions and signal-noise ratios. However, image quality is always a trade-off between the experimental needs and factors such as quantum yield, stability and specificity of the fluorescent markers, as well as optics, illumination, filters and detectors. Together, they define the signal quality and the size of the Point Spread Function (PSF) that collects the photon response of a single fluorescent emitter within the focal plane (Fink *et al.*, 1998; Kubitscheck, 2017).

A typical diameter of a PSF for an *in vivo* confocal microscopy setting is $\sim 0.25\ \mu$m for the *xy*-plane, and $\sim 0.8\ \mu$m for the *z*-axis (M1). This is about 50–160 times the thickness of a lipid bilayer of a eukaryotic cell membrane (~ 5 nm), whose orientation with respect to the focal plane and the PSF defines different acquisition scenarios. Fluorescence signals are integrated within the convolution of the PSF with the fluorescent intensity distribution, proportional to the density of fluorophores attached to or embedded in the membrane. In this regard, the effect of convolution for different orientations of giant unilamellar vesicle membranes with respect to the PSF has been discussed (Fidorra *et al.*, 2009). However, cellular membranes are more complex than model membranes: they present deformations like blebs, microvilli or protrusions which result in images with a plurality of signal patterns, and the accurate detection of photon activity and membrane morphology becomes difficult (Frangi *et al.*, 1998; Mosaliganti *et al.*, 2012). The precise localisation of a membrane sheet, especially when adjacent to a neighbouring membrane, becomes difficult, since blurry, missing or nonspecific membrane signals are present throughout the images (Fig. 1). It is frequent in multicellular aggregates that membranes appear adjacent along the *z*-axis, but clearly separated within the *xy*-plane due to the PSF shape (Mosaliganti *et al.*, 2012). In addition, for *in vivo* imaging of multicellular samples, especially in developing organisms, rapid events of cell reshaping and motion occur constantly, and varying fluorescence levels are observed due to different molecular expression timings (Pawley, 2006).

A first step towards resolving the localisation of membranes from fluorescence microscopy images is deconvolution. Deconvolution algorithms restore images based on likelihood criteria in order to correct for blurring (out-of-focus signals) and random noise, and to optimise the signal-noise ratio (Sarder & Nehorai, 2006). However, the deconvolved images are still diffraction limited according to Abbe's law: two membrane sheets that are closer than the full width at half maximum of the PSF cannot be resolved with conventional confocal microscopy. The observed phenomenon of varying intensity profiles due to the convolution of neighbouring membrane sheets with different orientations with respect to the PSF must be interpreted by a competent expert. However, deconvolution considers a 3D PSF and complementary data improves the likelihood estimation, and image quality in 2D can be enhanced significantly when intensity information above and below the respective *xy*-plane is available.

Following image deconvolution, segmentation algorithms separate images into Regions of Interest (ROIs) which define cells and background. Over the years, different algorithms for detection and segmentation of cellular membranes have been introduced (Table 1), but the detection and appropriate handling of cell contours for multiple cells in tissue and whole organisms have not been solved on a general level so far. Existing algorithms can be separated into pixel based and contour based approaches. A representative of pixel based approaches is the family of watershed algorithms (Beucher & Lantuéjoul, 1979; Bertrand, 2005; Mashburn *et al.*, 2012) where adjacency between ROIs in binary images can be defined and handled by neighbourhood criteria or chain codes at pixel level. However, a morphological characterisation of the ROIs that requires the length or the curvature of border segments lacks precision due to the discrete pixel representation. Some authors combine watershed based approaches with fine meshing approaches (Veldhuis *et al.*, 2017) to improve the membrane localisation. In addition, an adequate edge-enhancing filter to smooth and connect membranes must be applied to the intensity image prior to the watershed.

Contour based approaches like parametric active contours (Kass *et al.*, 1988) use image intensity gradient vector fields, such as the Generalised Gradient Vector Flow field $GGVF(I(x,$

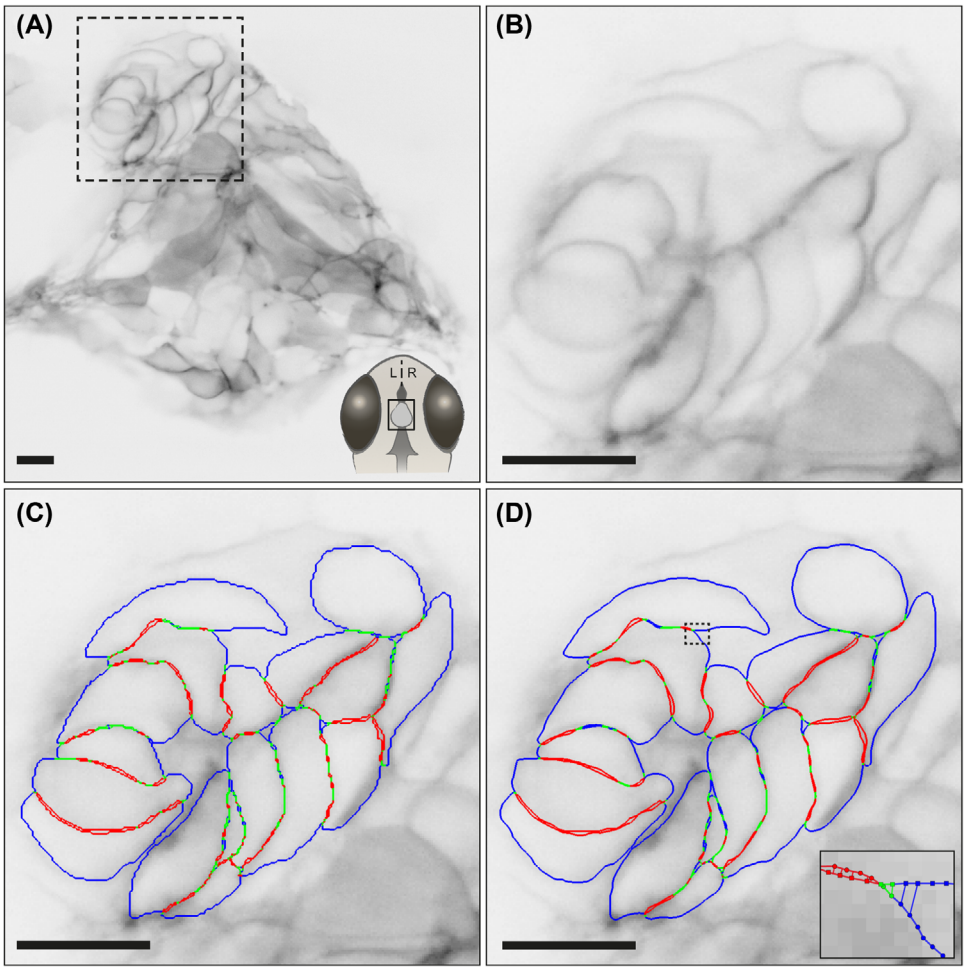

Fig 1. Optimised membrane segmentation and definition of overlapping, adjacent, and nonadjacent contour sections of neighbouring cells of the PpO. Spinning disc microscopy images of the PpO of a zebrafish transgenic *flh*::gap43-EGFP embryo were acquired at 38 hpf. Fluorescence intensities are shown in inverted greyscale. (A) 2D image slice from a 3D stack of the pineal complex. The scheme at the bottom right corner depicts the zebrafish embryo head with the pineal complex position and Left–Right (L|R) alignment within the central nervous system (black square). (B)–(D) Detail of the PpO cell membranes from the dashed square in (A). (C) Manually Outlined Contours (MOC) and (D) optimised Parametric Active Contours (PAC), with colour code for overlapping (red), adjacent (green) and nonadjacent (blue) contour sections, defined by an adjacency distance $d = 83$ nm. The insert in (D) shows the shortest distance between segments from two cell contours from the dashed rectangle (M5.1). Scale bars: 10 μm.

y)) (Xu & Prince, 1998a; Xu & Prince, 1998b), to attract contour vertices towards the membranes by balancing physical contour properties like elasticity or rigidity. A series of constraints define an energy functional and a final relaxation state of minimum energy that optimises the position of the final ROI contour in balance with the gradient vector field. Parametric active contours are optimised independently for each ROI; therefore, overlapping and adjacent contours need to be detected and corrected for neighbouring objects (McInerney & Terzopoulos, 1995; Namías *et al.*, 2016).

Implicit active contours or 'level sets' (Osher & Paragios, 2003) are based on global optimisation models combined with image intensities and/or intensity gradient terms into the minimisation function to guide the contour evolution. The quality of the segmentation depends on the homogeneity of the membrane signal and the boundary detector. In this regard, methods for membrane signal enhancement have been introduced and can be coupled to both implicit and parametric approaches (Frangi *et al.*, 1998; Mosaliganti *et al.*, 2012; Michelin *et al.*, 2014). Regularisation terms can be included in implicit models to control shapes and smoothness, but overlapping or unwanted merging of ROI contours can occur (Chan & Vese, 2001; Sarti *et al.*, 2002). Radon transform (Dzyubachyk *et al.*, 2010) and regularisation repulsion forces (Dufour *et al.*, 2011; Dufour *et al.*, 2017) can correct overlapping contours, but the results are straight lines, planes or nonadjacent ROIs that compromise cell morphology (Table 1).

Table 1. Handling of adjacent sections within different segmentation approaches.

Approach	Handling of adjacent sections
Watershed (Bertrand, 2005; Beucher & Lantuéjoul, 1979): Subdivides an image into a number of ROIs, following topographic profile transformations that generate digital elevation models on the basis of the image intensity pattern. The result is separated ROIs at pixel level.	+: Adjacency between objects can be defined and handled easily at pixel level. −: ROIs are defined at pixel level, border pixels must be defined by a neighbourhood criteria or chaincode algorithms. Limited morphological characterisation.
Automated cell morphology extractor, ACME (watershed based) (Mosaliganti *et al.*, 2012; Frangi *et al.*, 1998): Principal directions of intensity variations from the image enhance membrane detection in zones with weak signal intensities of adjacent membranes. The directions are used to locate the principal curvature of the membrane, reconstructing interfaces between adjacent cells.	+: Enhances weak membrane signals and applies morphological watershed. Multiscale approach. −: No direct characterisation of adjacent interface besides watershed separation. Robust morphological separation not ensured.
Real-time accurate cell-shape extractor, RACE (watershed based) (Stegmaier et al., 2016; Vachier & Meyer, 2005): Cell shape characterisation from membrane and nucleus segmentation similar to ACME. It uses morphological watershed with flooding of a viscous liquid. Works in in 2D/3D.	+: Enhances the membrane signal and applies morphological viscous watershed, therefore getting a smoother solution for low resolution/information boundaries. −: Same as ACME.
T-snakes (active contours) (McInerney & Terzopoulos, 1995): Grid-based model for contour merging/splitting. Grid recognises collision between snakes.	+: The grid either separates or fuses the contours in case of adjacency or overlapping, automatically discarding adjacency conflicts. −: No adjacency definition to resolve a shared section between touching ROIs.
Active contours without edges (active contours) (Chan & Vese, 2001): Curvature-driven contour evolution considering ROI interior properties. ROI boundary completion does not require strong intensity gradients.	+: Few parameters. −: No intrinsic handling of overlapping sections. No intrinsic adjacency detection (reliant on the intensity gradient).
Subjective surfaces (active contours) (Sarti *et al.*, 2002): Boundary completion with missing information. Contour perimeter minimisation term allows for boundary completion in absence of strong gradient. Requires initialisation from a point in the ROI interior.	Same as Active contours without edges.
3-D active meshes (active contours) (Dufour *et al.*, 2005; Dufour *et al.*, 2011): Discrete variational energy optimisation. Fast multiple coupled active contours with and without edges. More computationally costly than distance-based methods. Defines a repulsion term but without measuring the outcome.	+: Repulsion forces are exerted over overlapping contour zones. −: Adjacency separation not guaranteed.
Advanced level-set-based cell tracking (active contour-based) (Dzyubachyk *et al.*, 2010): Radon transform with active meshes. Separation planes are computed for touching ROIs with the Radon transform.	+: Separates adjacent cells using planes/lines (3D/2D). −: Lacks expressive separation to account for adjacent membrane curvatures.
Deformable model array (other) (Namías *et al.*, 2016): Pipeline of deformable and nondeformable models. Cooperative multiobject 2D/3D segmentation.	+: *Ad hoc* collision detection handling. −: Not implemented. Algorithms for contour stop/rollback only.

The aforementioned methods produce satisfactory results when ROIs present regular shapes (Baggett *et al.*, 2005; Luck *et al.*, 2005; Stegmaier *et al.*, 2005; Coelho *et al.*, 2009; Drelie-Gelasca *et al.*, 2009; Mosaliganti *et al.*, 2009), but fail for live imaging of developing organisms with complex morphology and acquisition conditions that do not permit to respect optimal image sampling criteria. A particular example is the 3D imaging of the Parapineal Organ (PpO) in developing zebrafish embryos. The small brain nucleus is located in the dorsal diencephalon, associated to the pineal complex. The PpO formation occurs between 26 and 48 hours post-fertilisation (hpf). Cells of the PpO re-arrange and form a rosette-like structure that detaches from the pineal complex and moves to the left side of the brain (Concha *et al.*, 2003; Härtel *et al.*, 2007; Regan *et al.*, 2009). During this process, cells change their shape and reorganise with respect to their neighbours. A quantitative view on cell morphology, membrane adjacency, reorganisation of cell and tissue topology, and cell neighbours, is the basis to understand the underlying mechanisms of the PpO asymmetric morphogenesis. This task depends on the additional challenge

of segmenting PpO cell membranes of highly variable shapes which are subject to rapid deformations and displacements of the cell borders, clustered cells, intrinsic variations of the transgenic fluorescent membrane signal, and variable image background. The combination of these factors results in subjective cell boundaries which depend on an expert criterion for a satisfactory segmentation.

In this work, we address the issue of detecting nonadjacent, adjacent, and overlapping contour sections for parametric cell contours. We introduce a geometrically consistent solution for a common shared contour of cell neighbours under the constraint of maintaining the overall contour morphologies. We introduce the ALgorithm for Piecewise Adjacent Contour Adjustment (ALPACA) that detects and adjusts contour sections within a defined adjacency distance *d*. ALPACA defines a polyline as an optimised shared contour section and solution for connecting adjacent and nonadjacent sections, under the constraint of preserving the underlying cell morphology. We apply and evaluate a combination of Parametric Active Contours (PAC) with ALPACA for the segmentation of PpO cell membranes in zebrafish embryos, acquired by 3D live spinning-disc microscopy. In order to assess the performance of ALPACA and the interexpert variation of Manually Outlined Contours (MOC) by independent experts, we present results from 51 cell borders during PpO formation, and a synthetic ground truth scenario of 88 hexagonal cells with defined Adjacent Edges (AE). We determine a series of indices for morphology and similarity of objects to test if cell shape and adjacency are preserved throughout the experiments.

Materials and methods

M1 Microscopy/image acquisition

Embryos were obtained by natural spawning from a *flh*:: gap43-EGFP transgenic zebrafish line (Concha *et al.*, 2003). The sample embryo was anesthetised (tricaine 0.003%, Sigma) and mounted in 1% low melting point agarose (Winkler). The PpO morphogenesis was observed using a spinning disc microscope (ZEISS; Jena, Ger./PerkinElmer; Waltham, MA, USA) under controlled temperature conditions (28°C). 3D Image stacks (8-bit single channel intensity $I \in [0, 255]$), were captured with a 40x (NA 1.2) water-immersion objective, excitation/emission wavelength at 488/505-560 nm, *xyz* stack of 768 × 768 × 69 voxels and 166 × 166 × 500 nm^3 voxel size. Raw images were deconvolved using Huygens Software (SVI, Hilversum, the Netherlands). Sampling distances were calculated with Nyquist rate and PSF calculator (https://svi.nl/NyquistCalculator).

M2 Synthetic image with hexagons of defined membrane adjacency

A 2D vector image for 88 hexagons was generated with Adobe Illustrator software (Adobe; San Jose, CA, USA), and rasterised to 768 × 768 pixels. Horizontal edges of the hexagons were 43 pixels long, diagonal edge length and pixel representation varied slightly due to the rasterisation algorithm. The membrane adjacency between hexagons was defined as follows: 11 hexagons with 6 Adjacent Edges (AE), 17 with 5 AE, 13 with 4 AE, 12 with 3 AE, 13 with 2 AE, 11 with 1 AE and 11 hexagons without AE (0 AE). The distances for hexagons with 0 AE to the next hexagon varied from 3 to 12 pixels. Edge/background intensity was set to 255/0 (8 bit). The image was convolved with the theoretical PSF calculated with Huygens Software for a pixel size identical to the *xy* microscope settings (166 × 166 nm^2), and re-scaled to 8 bit (Fig. S2A).

M3 Segmentation of cells and synthetic hexagons by manually outlined contours (MOC)

Membrane segmentation was performed for 17 cells of the PpO (a total of 51 MOC in consecutive *xy*-planes along the *z*-axis) and for 88 synthetic hexagons (M2), by three independent experts with more than two years of training in *in vivo* microscopy and manual segmentation of diverse cell structures. The contour of each object was outlined as a closed polygon using a digital Pen CTE-440 tablet (Wacom; Saitama, Japan). Binary ROIs were generated with a custom-made macro written for the Image SXM software program (Barrett, 2015).

M4 Parametric active contours (PAC)

The parametric active contour or 'snake' model (Kass *et al.*, 1988) defines contours as time-dependent parametric curves. Each ROI contour is defined by a curve $C = C(s)$ parameterised in space with $s \in [0;1]$. Relative to the contour curve, two internal and one external energy terms are weighted in the energy functional E:

$$E = E(C(s)) = \frac{1}{2}\int_s \alpha\left(\frac{\partial C}{\partial s}\right)^2 + \beta\left(\frac{\partial^2 C}{\partial s^2}\right)^2 ds + \kappa E_{ext}(C(s)).$$

The internal energy terms mimic physical contour properties of elasticity/contractility (with weight coefficient α) and rigidity (β); the external energy (κ) is derived from the image intensity gradient in order to drive the contour towards observed ROI edges (in this case, the generalised gradient vector flow (Xu & Prince, 1998a; Xu & Prince, 1998b)). A *force* balance equation to find the minima for the functional E is defined by (i) the Euler-Lagrange differential equation system (Kass *et al.*, 1988; Aubert & Kornprobst, 2006) and (ii) time dependency of the contour curve $C = C(s,t)$ with $t \in [0;\infty]$:

$$\gamma\frac{\partial C}{\partial t} = -\alpha\frac{\partial^2 C}{\partial s^2} + \beta\frac{\partial^4 C}{\partial s^4} + \kappa f_{ext}(C(s)).$$

The force balance is reached when the sum of the terms at both sides of the equation are equal to zero. The time derivative at the left side is introduced to iteratively deform the contour

from a given initial shape (automated or manual) towards a final equilibrium shape, according to the dynamics defined by the force terms. The coefficient values control the final equilibrium state of each contour. Additionally, the result depends on the numerical, discrete implementation of the evolution equation. The most common implementation is made with finite differences upon an ordered list of contour vertices V_j ($j = 1,2, \ldots n$) that form a closed polygon or open polyline by making $C = C(s,t) = \{V_j(x,y)\} = \{x_j(s,t),y_j(s,t)\}$. Each consecutive pair of vertices defines a segment that serves as the basis for adjacency detection and contour adjustment of neighbouring ROIs. A viscosity coefficient γ is included in the equation to control the evolution speed of the contour Δt. Convergence parameters serve as stopping criteria for iterative solvers: maximum iteration count, and/or contour displacement thresholds based on a given norm. After each iteration, the contour curve needs to be resampled to ensure a set of equidistant vertices for homogeneous parameterisation and numerical stability (see Fanani *et al.*, 2010) for examples of varying force coefficients on active contours for the segmentation of lipid monolayers). We modified the iterative solving scheme for energy minimisation of each contour in order to allow fixed contour vertices from shared sections.

$GGVF(I(x,y)) = [u(x,y), v(x,y)]$ is a vector field, calculated from the intensity gradients of an image $I(x, y)$ (Xu & Prince, 1998a; Xu & Prince, 1998b; Härtel *et al.*, 2007; Fanani *et al.*, 2010). First, an intensity gradient vector field $[I_x, I_y]$ is calculated from $I(x, y)$. The *edgemap* image $I_e = |I_x| + |I_y|$ highlights strong intensity transitions and is used as the basis for the computation of the *GGVF* field. The *GGVF* model implements an advection/diffusion model that propagates strong gradient vectors towards zones with low gradients. The algorithm for computing the vector field optimises an integral functional defined over the entire field, similar to the snake energy, by iteratively solving an Euler-Lagrange PDE system. The implemented *GGVF* algorithm permits control of how pronounced the rise/decay of the field will be (regularisation coefficient μ). Within our work, we used the following weight coefficients: elasticity $\alpha = 0.0002$, rigidity $\beta = 0.003$, *GGVF* image force field $\kappa = 0.0015$. Contour parameters: viscosity $\gamma = 1.0$, average segment length $ASL = 1$ pixel length (166 nm), maximum deformation iterations = 1000, convergence threshold = 2E-6 (average vertex displacement divided by contour perimeter). *GGVF* parameters: regularisation $\mu = 0.5$, iterations = 100.

M5 Algorithm for piecewise adjacent contour adjustment (ALPACA)

Input, output and intermediate steps of ALPACA are shown as a flowchart in Figure 2. The input consists of: (i) a fluorescence intensity Image $I(x,y)$, (ii) the Generalised Gradient Vector Flow field $GGVF(I(x,y)) = [u(x,y), v(x,y)]$ (optional), (iii) the adjacency distance threshold d set by an expert considering the spatial resolution limit of the specific microscope settings and the image quality, and (iv) a set of parametric contours $C_i(x,y)$. These can be obtained from an active contour approach (M4) optimised to represent the morphology of a subjacent ROI according to a ground truth (if available) or a reference segmentation by an expert, either from automatic or manual segmentation procedures (Härtel *et al.*, 2007; Fanani *et al.*, 2010) (Figs. 1C, D). In principle, the set of $C_i(x,y)$ can also derive from alternative methods to active contours.

On the basis of the set of $C_i(x,y)$ and d, ALPACA calculates the distance between neighbouring contour sections based on the segment-segment distance, and classifies nonadjacent, adjacent, and overlapping contour sections (M5.1, Figs. 1C, D). If no adjacent or overlapping sections exist, the output $C_i(x, y)$ is returned for further morpho-topological quantification. If adjacent or overlapping sections do exist, a calculation of a correspondence vertex mapping based on normalised segment lengths is performed (M5.3) and Shared Contour Sections are calculated by averaging the (x, y) positions of corresponding vertices. Next, the algorithm checks if nonadjacent contours exist (a ROI might consist of adjacent contours only). If not, $C_i^*(x, y)$ is returned. If nonadjacent contours do exist, Piecewise Parametric Active Contours $C_i^{**}(x, y)$ are calculated to connect nonadjacent and shared sections. For the data presented in this article, vertices of the calculated shared sections were fixed, and the nonadjacent sections re-adjusted under the initial active contour constraints that respect morphological features of the subjacent ROIs (M5.2, Figs. 3G, H). The use of *GGVF* is optional, and was not applied in the final relaxation in our examples. Finally, $C_i^{**}(x, y)$ is returned for further analysis.

In summary, ALPACA returns one of three possible outputs: (i) parametric contours $C_i(x,y)$ with no adjacent sections, (ii) parametric contours $C_i^*(x,y)$ where all sections fulfil the adjacency criteria and (iii) piecewise parametric contours $C_i^{**}(x,y)$ with sections that fulfil the adjacency criteria and sections that do not. The artefact of overlapping sections was corrected in $C_i^*(x, y)$ and $C_i^{**}(x, y)$, and the results fit the morphological constraints of the microscopic sample.

M5.1 Classification of adjacent, overlapping and nonadjacent contour sections within the adjacency distance d.

M5.1.a Adjacent contour sections of neighbouring ROI contours are sets of one or more consecutive segments (polylines) which lie at a distance equal or lower than the Adjacency Distance *d*. The minimum distance between each segment of a first contour and all the segments of a second contour is calculated by a segment-segment distance algorithm. The shortest Euclidean distance is taken from each of the two vertices of the first segment to the second segment and from each of the two vertices of the second segment to the first segment (de Berg *et al.*, 2008, inset in Fig. 1D).

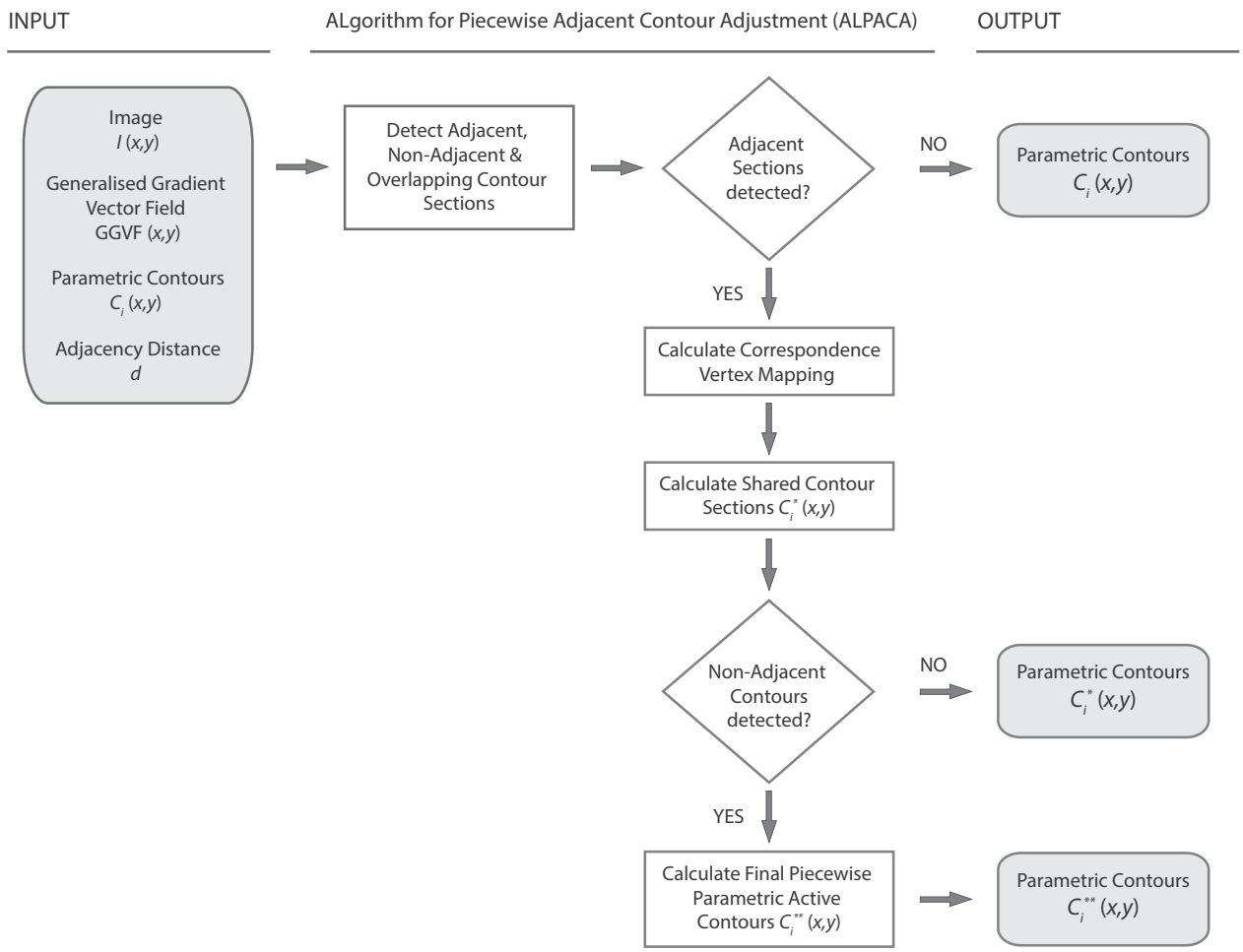

Fig 2. Membrane segmentation pipeline. Flowchart indicating input, steps of the Algorithm for Piecewise Adjacent Contour Adjustment (ALPACA), and the three possible outputs.

M5.1.b Overlapping contour sections of neighbouring ROIs are sets of one or more consecutive segments which lie within each other, independently of the Adjacency Distance *d*. Overlapping is detected by the Boost implementation of the Weiler–Atherton algorithm for polygon intersection (Weiler & Atherton, 1977; Boost 2017). Contour segments that belong to the intersections are labelled as overlapping segments and connected to overlapping sections.

M5.1.c Nonadjacent contour sections are contour sections that are neither adjacent nor overlapping.

M5.2 Shared contour section

Shared contour sections are defined for adjacent and overlapping contour sections of two neighbouring ROIs. A Correspondence Vertex Mapping (M5.3) is used to define a list of vertex pairs with one vertex from each ROI, and to average the position of each pair of vertices. The result is a common shared contour section (Figs. 3F, H) which depends on the selected mapping approach, and substitutes the former adjacent and overlapping contour sections of the corresponding ROI contours.

M5.3 Correspondence vertex mapping

The Correspondence Vertex Mapping for two contour sections returns as a list of paired vertices from each contour. We tested two approaches:

M5.3.a Euclidean Distance Correspondence Vertex Mapping.

i. The contour section with the higher number of vertices is selected as reference. If numbers are equal, the result is independent of the selection.
ii. The first two vertices of the polylines are connected, becoming the first pair of the correspondence list. The result is independent of the selection of the first or the last vertex.
iii. For each following vertex of the reference polyline, the closest vertex of the second polyline is detected. The paired

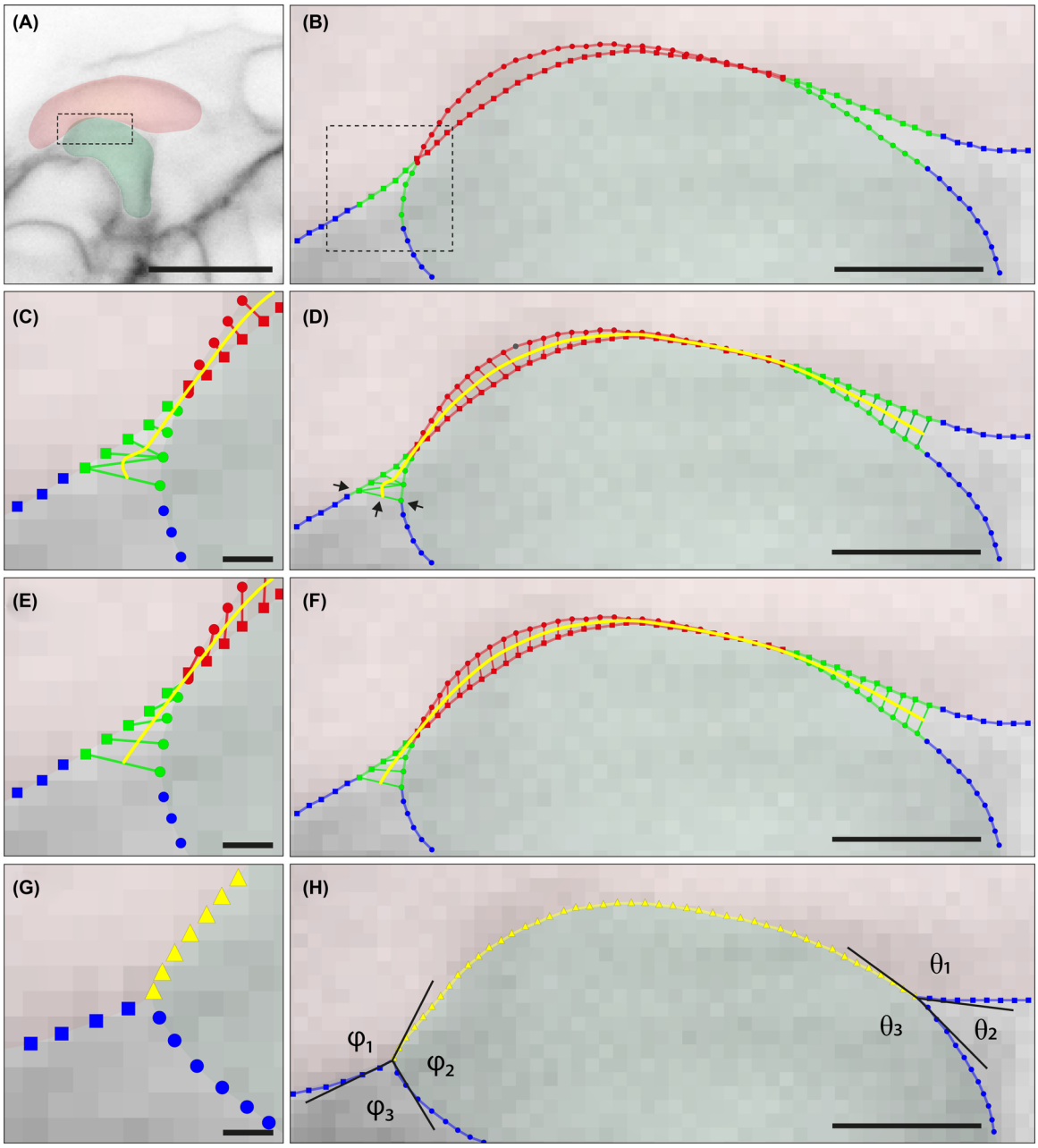

Fig 3. Normalised length based correspondence vertex mapping in combination with piecewise active contours lead to shared contour sections for morphology preserving cell contours. Scale bars in (A): 10 μm, (B/D/F/H): 2 μm, (C/E/G): 332 nm. Arrows in (D/F) mark the start vertices of each section. (A) Two neighbouring PpO cells (red and green) from the 2D image slice of Figure 1. Detail of the adjacent contour section within the dashed rectangle is shown in B–H. (B) Detail of adjacent (green), nonadjacent (blue), and overlapping (red) contour sections defined by d. (C)–(D) Shared contour section (yellow) calculated with the Euclidean Distance for Correspondence Vertex Mapping of the contour sections. (C) Detail of adjacent, nonadjacent and overlapping contour sections of the dashed rectangle in (B). The vertex mapping leads to undulating extremes in the shared section. (E)–(F) Shared contour section (yellow) calculated with the Normalised Length for Correspondence Vertex Mapping of the ROI contour sections. (E) Detail of adjacent, nonadjacent, and overlapping contour sections of the dashed rectangle in (B). The vertex mapping leads to smooth extremes in the shared section. (G)–(H) Piecewise active contours (yellow triangles and blue squares and circles) guarantee smooth transitions between adjacent and nonadjacent contours, and preserve the morphology of two neighbouring PpO cells. Angles of the triplet vertices at the contour junctions can be calculated by fitting straight lines to a selected number of contour vertices next to the tip (see representative lines for $\theta 1, \theta 2, \theta 3$ and $\varphi 1, \varphi 2, \varphi 3$). (G) Detail of the result for piecewise active contours from the dashed rectangle in (B).

vertices are added to the correspondence list consecutively.

iv. The last two vertices of the polylines are connected, becoming the last pair in the correspondence list.

M5.3.b Normalised Length Correspondence Vertex Mapping.

i. The length of each contour section is calculated as the sum of the length of its segments. The length of a segment is the Euclidean Distance between its two vertices.
ii. Each segment is normalised by the total length of its section, producing one-dimensional normalised vertex positions. The vertices of each section have a normalised length in the range [0; 1], with vertices at length 0 and 1 as start and end, respectively.
iii. One of the sections is taken as reference list to start the correspondence list. For sections with unequal numbers of vertices, the polyline with more vertices is used. The correspondence list is generated by advancing vertex by vertex from the reference list, matching with the closest vertex in the second list. The matching is made by comparing the normalised lengths of the vertices. The result is independent of the starting vertex.

M5.4 Piecewise parametric contours

As described before (M5) ALPACA returns one of three possible outputs: (i) parametric contours $C_i(x, y)$ without adjacent sections, (ii) parametric contours $C_i^*(x, y)$ where all sections fulfil the adjacency criteria and (iii) piecewise parametric contours $C_i^{**}(x, y)$ with sections that fulfil the adjacency criteria and sections that do not. For outputs (i) and (ii), there is no need for further adjustment of the ROI contours. For (iii), the shared contour sections (M5.2) are connected to the nonadjacent contour sections and form a new ROI contour. In order to produce smooth contours, we applied a piecewise active contour algorithm that fixed the vertices of the shared contour sections, but adjusted the nonadjacent contour sections under the constraints of the active contour approach. The result of the piecewise approach is shown in Figure 3(H).

M5.5 Software implementation

ALPACA was implemented within SCIAN-Soft, a custom-built software platform programmed in IDL 7.1.2 (ITT/ Harris; Boulder, CO, USA). Polygon intersection and distance computation algorithms (M4) were sourced from the C++ Boost library version 1.71.0 (Boost 2017), encapsulated in custom functions, and compiled as dynamic link libraries for IDL using Visual Studio 2010 version 10.0.40219 SP1Rel (Microsoft; Redmond, WA, USA) in order to be integrated with SCIAN-Soft. Computer: custom built, Intel Core i7 3930K CPU, 64GB RAM, 64-bit Windows 7 SP1 Operating System.

M6 Indices for morphology and similarity

M6.1 Morphological indices

Seven indices were defined to quantify the difference of the morphology of the ROIs before and after ALPACA, and the characteristics of the shared contour sections: relative area variation, relative perimeter variation, relative adjacent length variation, relative nonadjacent length variation, section distance, section curvature, section length and average segment length. The indices were calculated using n_1, as the number of shared contour sections; n_2 as: (i) each pair of cells adjacent in each shared contour section ($n_2 = 2n_1$) for relative area & perimeter variation, (ii) each ROI of the slice ($n_3 = 17$) for relative adjacent and nonadjacent length variations, and (iii) each shared contour section (n_1) for the rest. Two additional indices, Normalised Area and Normalised Perimeter, were defined for pairwise contour comparison between two experts or between an expert and the ground truth.

M6.1.a Perimeter and Area.

The total perimeter of a contour $C_i(x, y)$ was determined by the sum of the length of its segments. The Area of $C_i(x, y)$ was calculated with the Shoelace Algorithm for polygons (Braden, 1986).

M6.1.b Relative and Normalised Perimeter and Area Variation.

Relative Perimeter and Area Variations were determined on the basis of the original ROI contours $C_i(x, y)$, and one of the possible three outputs of ALPACA, $C_i^{out}(x, y) = C_i(x, y)$, $C_i^*(x, y)$, or $C_i^{**}(x, y)$ (M5, Fig. 2). Normalised Perimeter and Area Variations were determined on the basis of two contours for pairwise comparison, $C_{1/2,i}(x, y)$, either between experts or between an expert and the ground truth. Perimeter and Area were calculated as described above (M6.1.a).

- Relative Perimeter Variation:

$$Relative\ Perimeter\ Variation = \frac{Perimeter\left(C_i^{out}(x, y)\right)}{Perimeter\left(C_i(x, y)\right)}.$$

- Relative Area Variation:

$$Relative\ Area\ Variation = \frac{Area\left(C_i^{out}(x, y)\right)}{Area\left(C_i(x, y)\right)}.$$

- Normalised Perimeter Difference:

$$Normalised\ Perimeter\ Difference = \frac{\left|Perimeter\left(C_{1,i}(x, y)\right) - Perimeter\left(C_{2,i}(x, y)\right)\right|}{\max\left\{Perimeter\left(C_{1,i}(x, y)\right),\ Perimeter\left(C_{2,i}(x, y)\right)\right\}}.$$

- Normalised Area Difference:

$$Normalised\ Area\ Difference = \frac{\left|Area\left(C_{1,i}(x, y)\right) - Area\left(C_{2,i}(x, y)\right)\right|}{\max\left\{Area\left(C_{1,i}(x, y)\right),\ Area\left(C_{2,i}(x, y)\right)\right\}}.$$

M6.1.c Relative Adjacent and Nonadjacent Length Variation.

For each ROI contour, the relative length of the adjacent and nonadjacent sections was calculated as the sum of their segment lengths, and divided by the total contour perimeter. The variation was then calculated as the ratio between the relative lengths of the adjusted contours with respect to their original lengths. In order to consider sections with only one vertex, the half-length of extreme segments was also summed.

M6.1.d Section Distance.

The similarity indicator for section distance (Sim_D) was defined by the area ratio between contour sections as:

$$Sim_D = 1 - \frac{|Area_C\,(SC,\,AC_1) - Area_C\,(SC,\,AC_2)|}{Area_C\,(SC,\,AC_1) + Area_C\,(SC,\,AC_2)}.$$

- The Contour Area ($Area_C$) defined the area between the Shared Contour (SC) section and the Adjacent Contour (AC) sections from the first and second ROI contours (AC_1 and AC_2).
- The area between contour sections $Area_C(SC,\,AC_{1/2})$ was calculated by the Shoelace Algorithm (M6.1.a).

M6.1.e Section Curvature.

The similarity indicator for section curvature (Sim_K) was defined by the following steps:

- First, correspondence lists $v_l = 0 \ldots N_{i-1}$ between contour sections were defined as in M5.3 to allow for vertex by vertex comparisons.
- The Curvature (K) a of contour section was calculated for all of its vertices $v_l = 0 \ldots N_{i-1}$ using the differential curvature approximation (Yates, 1974), considering for each vertex v_l its neighbours v_{l+1} and v_{l-1}. For the first v_0 and the last vertex v_{Ni-1} of a contour section, the curvature cannot be determined due to missing neighbours.
- Sim_K was calculated as:

$$Sim_K = 1 - \frac{\left|\sum_l \Delta K_l\,(SC,\,AC_1) - \sum_l \Delta K_l\,(SC,\,AC_2)\right|}{\sum_l \Delta K_l\,(SC,\,AC_1) + \sum_l \Delta K_l\,(SC,\,AC_2)}.$$

- The difference of curvature (ΔK_l) was calculated as the sum of differences of curvature between the Shared Contour (SC) section and the Adjacent Contour sections (AC_1, AC_2).
- The difference was summed over all the vertices to obtain the value of Sim_K.

M6.1.f Section Length.

The similarity indicator for section length (Sim_L) was defined as:

$$Sim_L = 1 - \frac{|Length\,(SC)/Length(AC_1) - Length\,(SC)/Length(AC_2)|}{Length\,(SC)/Length(AC_1) + Length\,(SC)/Length(AC_2)}.$$

- The Length of contour sections SC, AC_1 and AC_2 were calculated as the sum of the length of the contour segments (M6.1.a).

M6.1.g Average Segment Length.

The similarity indicator for section average segment length (Sim_{ASL}) of a section was defined as:

$$Sim_{ASL} = 1 - \frac{\min\left\{\frac{ASL(AC_1)+ASL(AC_2)}{2},\,ASL\,(SC)\right\}}{\max\left\{\frac{ASL(AC_1)+ASL(AC_2)}{2},\,ASL\,(SC)\right\}}.$$

- ASL(Contour) was calculated by dividing the contour total length by the number of its segments.
- $ASL(AC_1)$ and $ASL(AC_2)$ were averaged and compared to $ASL(SC)$.

M6.2 Similarity indices

Several indices were calculated for the evaluation the variability/similarity of the manual contours, the segmented ROIs, the parametric contours, and ALPACA.

M6.2.a Dice Coefficient and Jaccard Similarity Index.

The dice coefficient DC($C_{1,i}$, $C_{2,i}$) (Dice, 1945; Sørensen, 1948; Coelho *et al.*, 2009) and the Jaccard Similarity Index JSI($C_{1,i}$, $C_{2,i}$) (Coelho *et al.*, 2009) for two contours $C_{1/2,i}(x, y)$, were implemented on the basis of the area definition (M6.1.a) and polygon intersection and union (M5.1.b):

$$DC\,\left(C_{1,i}, C_{2,i}\right) = \frac{2^*\,Area\,\left(C_{1,i} \cap C_{2,i}\right)}{Area\,\left(C_{1,i}\right) + Area\,\left(C_{2,i}\right)},$$

$$JSI\,\left(C_{1,i}, C_{2,i}\right) = \frac{Area\,\left(C_{1,i} \cap C_{2,i}\right)}{Area\,\left(C_{1,i} \cup C_{2,i}\right)}.$$

For both indices, values range within [0; 1] (no overlap/perfect match).

M6.2.b Hausdorff Distance.

The Hausdorff Distance HD($C_{1,i}$, $C_{2,i}$) (Atallah, 1983) for two contours $C_{1/2,i}(x, y)$ was calculated based on the Distance $D(k)$ between polygon segments (Baggett *et al.*, 2005):

$$HD\,\left(C_{1,i}, C_{2,i}\right) = \max\left\{D\,(k) : C_{1,i_k} \neq C_{2,i_k}\right\}.$$

A low HD value indicates a close distance between the compared contours, with 0 as the minimum possible value for a perfect match.

M6.2.c Normalised Sum of Distances.

The Normalised sum of distances NSD($C_{1,i}$, $C_{2,i}$) (Coelho *et al.*, 2009) accounts for the accumulated distances from nonoverlapping pixels enclosed by contours $C_{1,i}$ and $C_{2,i}$. Values range within [0;1] (perfect match/no overlap). NSD($C_{1,i}$,$C_{2,i}$) was calculated on the basis of the pixel representation of each contour and interior area:

$$NSD\left(C_{1,i}, C_{2,i}\right) = \frac{\sum_k \left[C_{1,i} \neq C_{2,i}\right]^*\,D\,(k)}{\sum_k D\,(k)}.$$

Results and discussion

During cell migration and tissue organisation, the adjacency of cells and the direct contact between cell membranes mediate the type and strength of biochemical and mechanical interactions. Examples of contact mediated inhibition during cell locomotion are summarised in the recent review on the work of Abercrombie by Roycroft & Mayor (2018). Cell–cell collision can stimulate the formation of protrusions and migration in the opposite direction of the contact site. On the contrary, it has been reported that loss of collisions between cancer and healthy cells is associated with metastasis. The quantification of adjacency is also important to understand tissue–tissue interactions, for example, between the extra-embryonic epithelial enveloping cell layer and the mesenchymal embryonic cell layer during early development of annual killifish (Reig *et al.*, 2017). Here, the enveloping layer is used by the embryonic cells as a substrate for migration, directing the spreading of the embryonic tissue. Tissue–tissue interaction mediated by cell adhesion and tension relies on the ability of embryonic cells to couple motility to nonautonomous signals from the expanding enveloping layer.

The detection and quantification of adjacent and nonadjacent cell membranes opens the possibility to obtain and study a number of morphological aspects of cell-cell interaction, including number and temporal organisation, membrane morphology, angles formed at membrane junctions between two or more cells and the number and morphology of cellular protrusions. These morphological aspects are key information that allows a better understanding of cell–cell communication and the coordination of cell collective phenomena during morphogenesis, organogenesis, injury response or disease progression/treatment (Friedl & Gilmour, 2009; Rørth, 2009; Castañeda *et al.*, 2014). The detection and quantification of intercellular junctions is also relevant, since they provide information about the integrity to epithelia and other tissues, and the mechanical machinery necessary to execute morphogenetic and homeostatic intercellular rearrangements to coordinate tissue architecture with behaviour (Yap *et al.*, 2018).

Figure 1 shows 2D data of a 3D time series acquired to study the dynamics of the PpO morphogenesis. For the identification of cell membranes, spinning disc microscopy imaging was performed with *flh*::gap43-EGFP transgenic fish embryos. During PpO morphogenesis, 12–18 neuroepithelial adjacent cells form a rosette-like structure that detach from the pineal complex to form a small nucleus on the left side of the embryonic zebrafish brain (Concha *et al.*, 2003; Härtel *et al.*, 2007; Regan *et al.*, 2009). Imaging characteristics and quality shown in Figure 1 represent typical scenarios for *in vivo* experiments that focus on collective cell migration and tissue morphogenesis during embryonic development (Fig. 1A), combining the use of fast microscopy and fluorescent membrane proteins to outline the form of living cells and tissue (Lecaudey *et al.*, 2008; Richardson *et al.*, 2016; Reig *et al.*, 2017; Sanchez-Corrales *et al.*, 2018). The selected pixel size (166×166 nm) is about 3 times the suggested Nyquist rate of 50 nm (see M1). However, fast *in vivo* imaging is a trade-off between maximising resolution, field of view, fluorescence intensity, minimising photon damage, bleaching, and signal-noise ratio. For the presented experimental conditions, the Nyquist rate cannot be kept and a rate of 166 nm was selected.

Figure 1(B) shows membrane signals that vary in peak intensity and the width of the Gaussian intensity profile in the *xy*-plane. The variations can be explained by the different orientations of the membrane sheets with respect to the PSF: (i) membrane sheets oriented vertically with respect to the focal *xy*-plane lead to relatively 'thin' membrane profiles with high intensities, since fluorescence signals are integrated along the membrane sheet, collinear to the elongated *z*-axis of the PSF; (ii) membrane sheets oriented horizontally to the focal plane lead to 'thick' membrane profiles with relatively low intensities, since the intersection between the membrane sheet and the PSF reaches a minimum and (iii) membrane sheets oriented diagonally with respect to the *xy* plane of the PSF lead to 'intermediate' membrane profiles and signal intensities (Fidorra *et al.*, 2009; Mosaliganti *et al.*, 2012). In addition, membrane undulations, protein expression timings, and the dynamic organisation of protrusions add different intensity patterns to the image, and the direct, automated segmentation of cell membranes within the described conditions has not been fully solved so far (Mosaliganti *et al.*, 2012; Stegmaier *et al.*, 2016; Dufour *et al.*, 2017).

For image data shown in Figure 1, MOC are the only choice to obtain a first, rough approximation of cells and membranes, especially when the confluence and morphological complexity of the cells prevents the success of automated segmentation (Figs. 1A–C). Cell borders cannot be identified unequivocally in all parts of the image. The formation of protrusions in different directions, in addition to weak membrane signals, present a scenario where only an experienced investigator can take decisions to manually outline the best possible contours (M3). Naturally, the human bias and errors are intrinsically included. In scenarios with missing intensity information, MOC present a possible approximation. In Figure S1, similarities and differences generated by three independent experts are shown for $n = 17$ cell contours, and quantified for $n = 51$ PpO cell contours (Table S1). Three experts identified an equal number of cells with a very similar overall organisation and cell morphology. The average difference for the cell area is below 10%, and for the perimeter, below 8%, from the pairwise comparisons performed with MOC, PAC and ALPACA. The Dice/Jaccard and NSD similarity indices indicate an equivalent of similarity above 90%, 80% and 90% respectively. A Hausdorff Distance of ~ 7 pixels (1 μm) also supports a high similarity for MOC, PAC and ALPACA.

In a different scenario, we tested the interexpert variation of MOC and the deviation of expert drawings with PAC, and ALPACA within a synthetic, PSF-convolved ground truth image

(M2, M3). Figure S2 shows 88 hexagons with well-defined areas, edge length and Adjacent Edges (AE = 0,1, ... 6); both, MOC and ALPACA contours exhibit almost perfect alignment with the subjacent hexagon borders for all experts (Figs. S2B, C). Figure S2(D) shows a nearly perfect correlation of the AE values calculated from ALPACA contours with the ground truth AE values. Morphological and similarity indices shown in Tables S2 and S3 indicate nearly perfect match with the ground truth hexagons, and a very low interexpert variation for MOC, PAC, and ALPACA. The mean differences for area and perimeter are below or equal to 1% for pairwise comparison of expert MOC with the ground truth data. For the interexpert variation of MOC, the mean difference for the quantification of cell area is below 1.5%, and for the perimeter, below 1%. After ALPACA, the mean variations remain similar, but increased standard deviation values are observed in the morphological indices.

For all experts, MOC deviate from the predominantly smooth, curved membrane pattern in different parts of the image (Fig. 1C, Figs. S1A, D, G), and overlapping contours cannot be avoided. PAC are a powerful tool for the correction of small deviations from a membrane signal and pulse driven undulations of MOC. Vector fields attract contour vertices according to the intensity profile of the membranes, while the contour smoothness and shape is balanced by physical properties like elasticity or rigidity. PAC have shown excellent results for the segmentation of contours in different experimental systems and settings (de Tullio *et al.*, 2007; Härtel *et al.*, 2007; Fidorra *et al.*, 2009; Fanani *et al.*, 2010; Chang *et al.*, 2014; Bustos *et al.*, 2017). For PpO cells, Figure 1(D) and Figures S1(B), (E), (H) show the results of PAC for optimised membrane segmentation (M4) together with the detection of overlapping, adjacent, and nonadjacent contours within the distance criteria established by the selected adjacency distance $d = 83$ nm. The Dice/Jaccard and NSD values between expert MOC are all within the ~90% similarity range for the E1/E2 comparison; 82%, 81% and 92% for the E1/E3 comparison, and 89%, 81% and 93% for the E2/E3 comparison. The measured distance lies below 7 pixels (~1 μm) for E1/E2, ~8 pixels (1.1 μm) for E1/E3 and ~6 pixels (0.9 μm) for the E2/E3. The measured morphological indices for PAC were above 80% for the three comparisons. The similarity indices lie within 80% and 90%, and the Hausdorff Distance is below 7 pixels (~1 μm). The rest of the measurements in Table S3 show that both PAC and ALPACA preserve this small variability between experts within the same range.

The results of the ALPACA (M5, Fig. 2) are shown for two neighbouring PpO cells in Figure 3. For adjacent (green), nonadjacent (blue), and overlapping (red) membrane sections, ALPACA calculates a solution for a common, shared contour section on the basis of the Euclidean Distance Correspondence Vertex Mapping (M5.3.a, Figs. 3C, D) and the Normalised Length Vertex Mapping (M5.3.b, Figs. 3E, F). As Figures 3(E), (F) show, only the Normalised Length Correspondence Vertex Mapping leads to smooth shared contour sections for adjacent and overlapping membrane sections, avoiding undulations that can be observed at the tips of the sections in selected cases (see representative example in Figs. 3C, D). Finally, ALPACA connects the tips of the nonadjacent contour sections with the common shared contour section, and applies piecewise parametric active contour relaxation exclusively to the nonadjacent contours in order to produce smooth transitions between adjacent and nonadjacent contours (Figs. 3E, F). From the new contour solution presented in Figures 3(G), (H), the section length of adjacent versus nonadjacent membrane sections could be calculated together with morphological descriptors. Angles of the triplet vertices and the corresponding cell contours can be determined by standard fitting of straight lines or circular arcs to a number of contour vertices in proximity to tips (Fig. 3H). The improved cell–cell and cell–medium contours can also improve the estimation of angles between adjacent cells in 2D and should provide a more solid basis for force inference techniques that allow the estimation of tension maps in 2D and 3D (Brodland *et al.*, 2014; Veldhuis *et al.*, 2017). The Dice/Jaccard similarity indices and NSD values between expert ALPACA are in the 80% and 90% similarity range for the three comparisons The Hausdorff Distance remains below 7 pixels (~1 μm), supporting the observation of a high similarity of the ALPACA output, and a very similar variability between experts.

The free parameters of the active contour model allow optimisation of the contours for a plurality of shapes such as cellular membranes. Since we are not aware of a biologic sample that could fulfil the criteria of an acceptable ground truth for *in vivo* microscopy and exact localisation of the membrane sheets, it is not possible to define indicators such as the Hausdorff Distance or Dice Coefficient (Chang *et al.*, 2014) for the adjusted PpO cell contours. We propose a series of quality indicators to characterise adjusted shared sections and ROI contours (Figs. 4, 5). Figure 4 shows that distance (Fig. 4A) and curvature (Fig. 4B) of a sample shared contour section are balanced with respect to the adjacent and overlapping contour sections. The differences of the distance indicators that compare the shared contour section to each of the original ROI sections are within the size of the symbols used in the plot except for the first two vertex positions (compare Fig. 4A with Figs. 3E, F). The curvature plot of the shared contour section calculated with the Normalised Length Based Correspondence Vertex Mapping with respect to each of the original ROI contour sections (Fig. 4B) shows that the curvature of the shared contour section remains within the curvature values of the original ROI contour sections. A bias towards either one of the original contour section curvatures cannot be observed. It is, however, impossible to provide a perfect match of the shared contour section with respect to the distance and the curvature, since position and curvature are not independent parameters. However, the visual impression of the position of the vertices (Figs. 3E–H) combined with

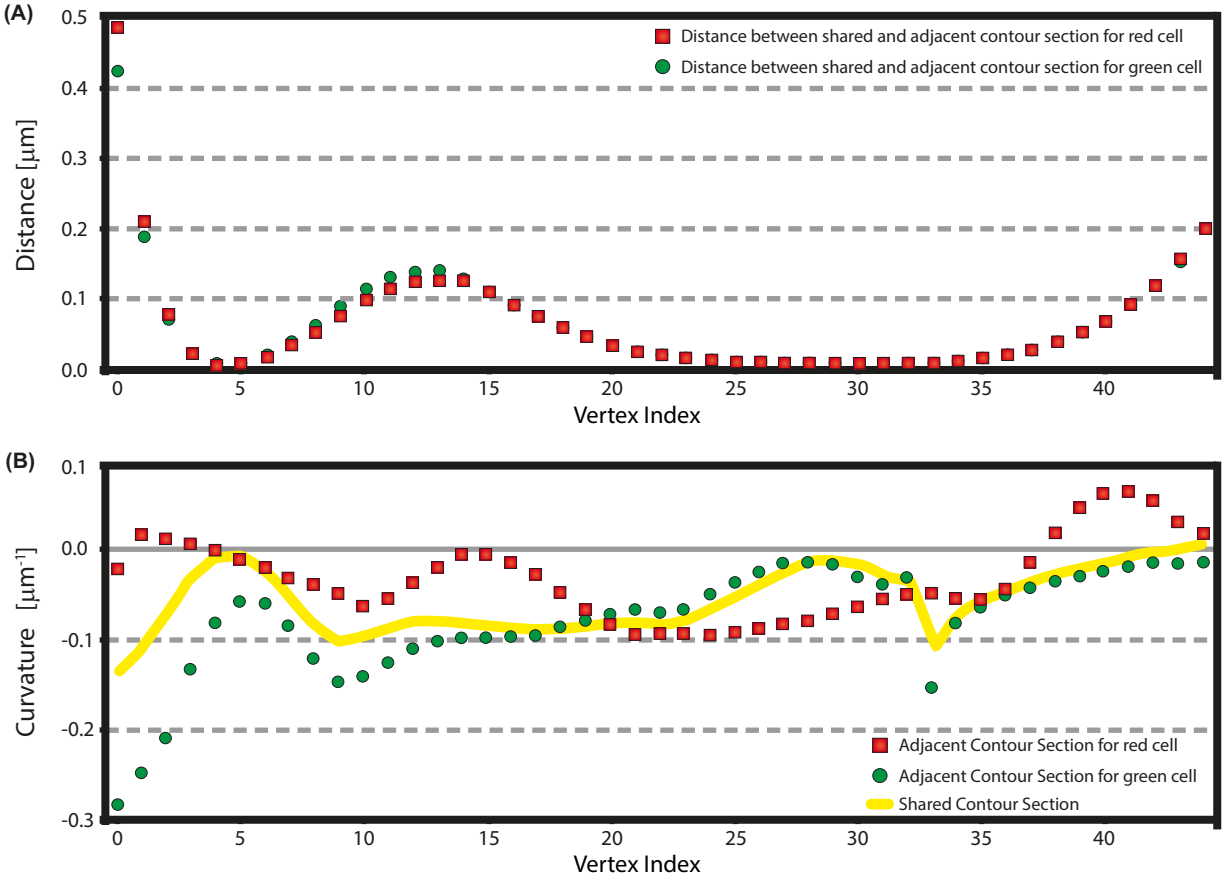

Fig 4. Distance and curvature of shared contour section calculated by ALPACA are balanced with respect to the adjacent and overlapping contours. Distance and curvature of the shared contour section and the adjacent contour sections are plotted as a function of the vertex index for the green and red cell contours shown in Figure 3 (see also M6.1.d-e). The vertex index 0 is indicated by the arrows in Figure 3(F). (A) Distances between the shared and the adjacent and overlapping contour sections of the red and green cells are plotted as red squares and green dots. A maximum difference of 485 nm was detected for the first vertex (index 0). (B): Curvature plot of the shared contour section (yellow line) and the adjacent and overlapping contour sections of the red and the green cell are plotted as red squares and green dots, respectively. Positive and negative curvature signs were assigned to counter clockwise and clockwise section turns, respectively.

the subjective quality indicators for distance and curvature (Fig. 4) satisfy our expectations for shared cell contours in general.

We measured the variation of morphological indices for the ROI contours and shared sections with dependence of the Adjacency Distance *d*. Figure 5 and Table 2 present relative variations of a total of seven morphological indices for the PpO cells after the application of ALPACA with selected adjacency distances ($d = 83, 166$ and 332 nm). The distances selected are subject to the features of the cell contours before the adjacency correction (M6.1.d-g). The relative area and perimeter variations start below 1, which is expected for ROIs with highly overlapping contours (red contour sections in Fig. S1), and tend to rise slightly with increasing *d*. This can be explained by the adjacency condition established by ALPACA at the interface of adjacent and nonadjacent contour sections. First, the adjacency condition forces the shared contour to balance the positions of both adjacent contour sections (Figs. 3E–H). This leads to shorter shared contour sections relative to both adjacent contour sections (compare Figs. 3E–H to Fig. 4 and Table 2). When *d* increases, the smoothness condition for the nonadjacent contours at the tips of the shared sections starts to add length to the contours. However, the increase is marginal within the tested range for *d* with respect to the overall contour morphology (Fig. 4, Table 2). The relative increase in ROIs with short nonadjacent sections is higher, up to ~20% (data not shown). All further morphological indices for section distance (Sim_D), section length (Sim_L), average segment length (Sim_{ASL}) and section curvature (Sim_K) show deviations from the mean values below 10% with respect to the original contour sections (Fig. 5). The indices increment with increasing *d*, which does not surprise, since the adjacent contour sections enlarge with *d*. A small number of outliers appear for the section curvature index, for short contour sections of dissimilar shapes

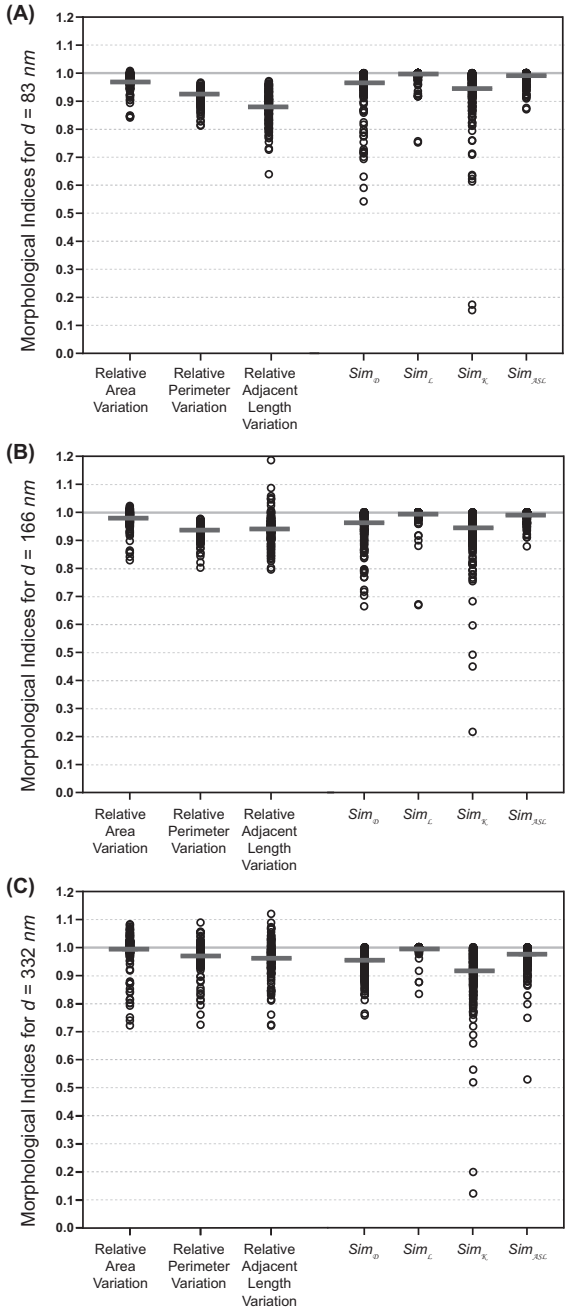

Fig 5. Morphological indices for increasing Adjacency Distance $d = 83$, 166, and 332 nm (A–C) of PpO cell contours after the application of ALPACA. Three morphological indices (relative area, perimeter, and adjacent length variation) quantify the deviation of the adjusted contours relative to the initial ROI contours, and four similarity indices (Sim_D, Sim_L, Sim_K, Sim_{ASL}) compare shared sections with their respective adjacent/overlapping sections (descriptions in M6.1.c–g). Indices were normalised with respect to the initial ROI contours which are set to 1. Aligned scatter plots (open circles, bars for mean values) contain data for each of the 51 cells with respect to its corresponding neighbours (see M6.1 for definition). Section similarity indices were computed from the detected shared sections.

whose adjusted shared section is not always able to compensate equally (not shown).

In addition to the parameters of the active contour approach (M4), the adjacency distance d is the only free parameter within ALPACA. Considering the varying conditions for *in vivo* experiments with cells, tissue, or organisms, and the heterogeneous geometries of membrane sheets with respect to the PSFs of different microscopic settings, d has to be adjusted for an optimal overall solution. The selection of d depends on the microscopic acquisition limits and the quality of the initial contours $C_i(x, y)$ that can be defined either automatically or manually. Figure 6 shows adjacent and nonadjacent cell membranes, and the solution calculated by ALPACA for $d =$ 83 nm. This condition for d corresponds to ~1.7 times the recommended sampling distance for the image acquisition in the xy-plane ($d = 50$ nm). Since mean variations of the morphological features of the cells in response to ALPACA are small for $d = 83$, 166 or 332 nm, the experienced researcher has to take a decision based on the visual perception of the resulting adjacent and nonadjacent sections and the variation of morphological features subject to each specific experimental question. The visual perception of the solution for the cell contours in Figure 6 is convincing. In the absence of a ground truth sample, different solutions for d close to the resolution limit should be tested and analysed. Results can be reported for a single d value, or a range of d values to evidence the robustness of the calculated data for adjacent and nonadjacent sections.

In summary, we show that the presented algorithm detects and corrects adjacent, nonadjacent, and overlapping contours in 2D within a selected adjacency distance d. ALPACA calculates shared contour sections and replaces adjacent and overlapping sections of neighbouring cell contours while minimising alterations of the original contour characteristics. Furthermore, ALPACA presents piecewise active contour solutions for pairs of cells that share one or more adjacent sections. Adjacent and nonadjacent sections are connected with curvature-preserving contours to maintain the overall cell morphology. The corrected 2D contours can set the basis to improve the representation of cells as 3D surfaces, the estimation of forces from contour parameters, or improve the tracking of contours in combination with previously published approaches (Mosaliganti *et al.*, 2009; Mashburn *et al.*, 2012; Mosaliganti *et al.*, 2012; Namías *et al.*, 2016; Stegmaier *et al.*, 2016; Veldhuis *et al.*, 2017). We are presently evaluating the implementation of ALPACA for FIJI (https://fiji.sc) or Icy (http://icy.bioimageanalysis.org), and prepare a version for IPOL (www.ipol.im) to provide source code for algorithm design within reproducible research. We currently provide access to our Internet repository with IDL sourcecode, together with the compiled libraries through GitHub (https://github.com/scianlab/sciansoft).

Table 2. Variation of morphological indices for increasing Adjacency Distance d.

	$d = 83$ nm $n_1 = 3 \times 51$ cells $n_2 = 294$ shared sections	$d = 166$ nm $n_1 = 3 \times 51$ cells $n_2 = 265$ shared sections	$d = 332$ nm $n_1 = 3 \times 51$ cells $n_2 = 281$ shared sections
RAV(n_1)	$0.969 \pm 0.031/0.003$	$0.978 \pm 0.032/0.003$	$0.996 \pm 0.010/0.001$
RPV(n_1)	$0.924 \pm 0.028/0.002$	$0.936 \pm 0.028/0.002$	$1.005 \pm 0.008/0.001$
RALV(n_1)	$0.882 \pm 0.058/0.005$	$0.941 \pm 0.017/0.004$	$0.986 \pm 0.051/0.004$
RNALV(n_1)	$0.969 \pm 0.031/0.003$	$0.923 \pm 0.143/0.012$	$1.082 \pm 0.351/0.028$
$Sim_D(n_2)$	$0.965 \pm 0.068/0.004$	$0.962 \pm 0.057/0.003$	$0.952 \pm 0.044/0.003$
$Sim_L(n_2)$	$0.993 \pm 0.024/0.001$	$0.993 \pm 0.031/0.002$	$0.997 \pm 0.016/0.001$
$Sim_K(n_2)$	$0.944 \pm 0.090/0.005$	$0.944 \pm 0.084/0.005$	$0.914 \pm 0.095/0.006$
$Sim_{ASL}(n_2)$	$0.997 \pm 0.019/0.001$	$0.989 \pm 0.017/0.001$	$0.972 \pm 0.041/0.003$

RAV, relative area variation; RPV, relative perimeter variation; RALV, relative adjacent length variation; RNALV, relative nonadjacent length variation. 17 PpO cell membrane contours along three z-slices were measured from ALPACA, upon the MOC of three independent experts. The number of shared sections (n_2) varies according to the value of d (M6). Mean ± SD/SE values are shown.

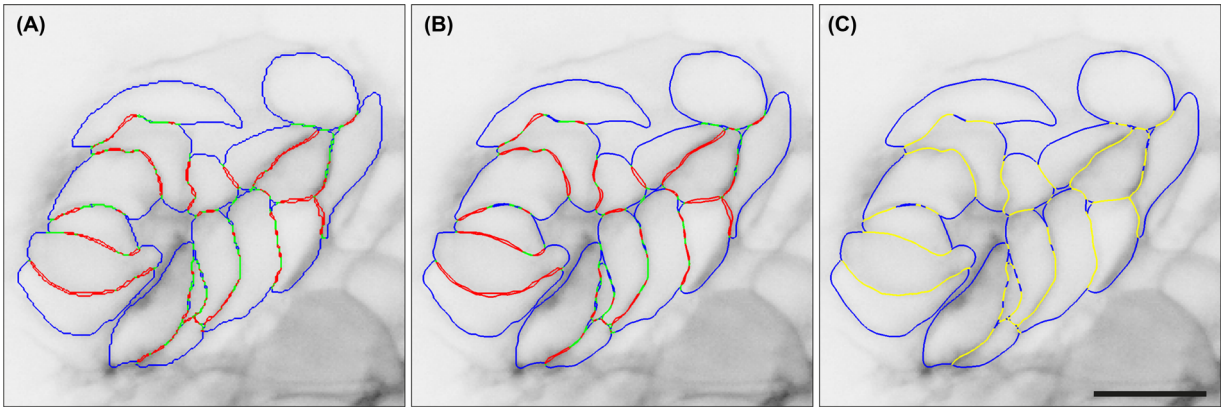

Fig 6. Optimised detection and separation of adjacent and nonadjacent cellular membranes with an adjacency distance $d = 83$ nm. (A) Manually Outlined Contours (MOC) and (B) optimised Parametric Active Contours (PAC) with adjacent (green), nonadjacent (blue), and overlapping (red) contour sections detected by ALPACA are plotted on top of the 2D image slice $I(x, y)$ from Figure 1. (C) Final adjustment of nonadjacent (blue) and adjacent (yellow) contour sections $C_i^{**}(x, y)$ are plotted after application of ALPACA. Scale bar: 10 μm.

Acknowledgements

This work was supported by the Chilean Millennium Scientific Initiative ICM P09-015-F to MLC, IC, JJ-W, SH, FV; CONICYT PhD scholarships to JJ-W; FONDECYT 11170475 to IC, VC; FONDECYT 1181823 to IC, CGL, VC, KP, MLC, SH; FONDECYT 3160421 to KP; FONDECYT 1161274 to MLC, SH; FONDECYT Ring Initiative ACT-1402 to MLC, SH; FONDECYT Ring Initiative ACM170003 to SH; FONDAP 15150012 to MLC; ANID Ring Initiative ACT-192015 to MLC; DAAD 57220037 & 57168868, CORFO 16CTTS-66390 to SH.

References

Atallah, M. J. (1983) A linear time algorithm for the Hausdorff distance between convex polygons. *Info. Process. Lett.* **17**, 207–209.

Aubert, G. & Kornprobst, P. (2006) *Mathematical Problems in Image Processing: Partial Differential Equations and the Calculus of Variations. Applied Mathematical Sciences*, vol. **147**, 2nd edn. Springer, New York, NY.

Baggett, D., Nakaya, M. A., McAuliffe, M., Yamaguchi, T. P. & Lockett, S. (2005). Whole cell segmentation in solid tissue sections. *Cytometry A* **67**, 137–143.

Barrett, S. (2015) Image SXM. Freeware web-downloadable application. http://www.ImageSXM.org.uk.

Bertrand, G. (2005) On topological watersheds. *J. Mathemat. Imag. Vision* **22**, 217–230.

Beucher, S. & Lantuéjoul, C. (1979) Use of watersheds in contour detection. In *Proceedings of the International Workshop in Image Processing CCETT/IRISA*, Rennes, France.

Boost (2017) Boost C++ Libraries. http://www.boost.org/. Last accessed 2019-01-21.

Braden, B. (1986) The surveyor's area formula. *Coll. Mathem. J.* **17**, 326–337.

Brodland, G.W., Veldhuis, J. H., Kim, S., Perrone, M., Mashburn, D. & Hutson, M. S. (2014) CellFIT: a cellular force-inference toolkit using curvilinear cell boundaries. *PLoS One* **9**, 1–15.

Bustos, F. J., Ampuero, E., Jury, N. *et al.* (2017) Epigenetic editing of the Dlg4/PSD95 gene improves cognition in aged and Alzheimer's disease mice. *Brain* **140**, 3252–3268.

Castañeda, V., Cerda, M., Santibáñez, F. *et al.* (2014) Computational methods for analysis of dynamic events in cell migration. *Curr. Mol. Med.* **14**, 291–307.

Chan, T. F. & Vese, L. (2001) An active contour model without edges. *IEEE Transact. Image Process.* **10**, 266–277.

Chang, V., Saavedra, J., Castaneda, V., Sarabia, L., Hitschfeld, N. & Härtel, S. (2014) Gold-standard and improved framework for sperm head segmentation. *Comp. Methods Progr. Biomed.* **117**, 225–237.

Coelho, L. P., Shariff, A., & Murphy, R. F. (2009) Nuclear segmentation in microscope cell images: a hand-segmented dataset and comparison of algorithms. In *Proceedings of the 6th IEEE International Symposium on Biomedical Imaging: From Nano to Macro, ISBI*. Boston, MA, USA. pp. 518–521.

Concha, M. L., Russell, C., Regan, J. C. *et al.* (2003) Local tissue interactions across the dorsal midline of the forebrain establish CNS laterality. *Neuron* **39**, 423–438.

de Berg, M., Cheong, O., van Kreveld, M. & Overmars, M. (2008) *Computational Geometry: Algorithms and Applications*, 3rd edn. Springer-Verlag, Berlin-Heidelberg.

de Tullio, L., Maggio, B., Härtel, S., Jara, J. & Fanani, M. L. (2007) The initial surface composition and topography modulate sphingomyelinase-driven sphingomyelin to ceramide conversion in lipid monolayers. *Cell Biochem. Biophys.* **47**, 169–177.

Dice, Lee R. (1945) Measures of the amount of ecologic association between species. *Ecology* **26**, 297–302.

Drelie-Gelasca E, Obara B, Fedorov D, Kvilekval K, Manjunath B. (2009). A biosegmentation benchmark for evaluation of bioimage analysis methods. *BMC Bioinformat.* **10**, 368–380.

Dufour, A., Shinin, V., Tajbakhsh, S., Guillén-Aghion, N., Olivo-Marin, J.-C. & Zimmer, C. (2005) Segmenting and tracking fluorescent cells in dynamic 3-D microscopy with coupled active surfaces. *IEEE Transact. Image Process.* **14**, 1396–1410.

Dufour, A., Thibeaux, R., Labruyere, E., Guillen, N. & Olivo-Marin, J. (2011) 3-D active meshes: fast discrete deformable models for cell tracking in 3-D time-lapse microscopy. *IEEE Transact. Image Process. IEEE Transact. Image Process.* **20**, 1925–1937.

Dufour, A. C., Jonker, A. H. & Olivo-Marin, J.-C. (2017) Deciphering tissue morphodynamics using bioimage informatics. *Philos. Transact. R. Soc. Lond. B: Biol. Sci.* 20150512.

Dzyubachyk, O., van Cappellen, W. A., Essers, J., Niessen, W. J. & Meijering, E. (2010) Advanced level-set-based cell tracking in time-lapse fluorescence microscopy. *IEEE Transact. Med. Imag.* **29**, 852–867.

Fanani, M. L., Härtel, S., Maggio, B., de Tullio, L., Jara, J., Olmos, F. & Oliveira, R. G. (2010) The action of sphingomyelinase in lipid monolayers as revealed by microscopic image analysis. *Biochim. Biophys. Acta (BBA) – Biomembr.* **1798**, 1309–1323.

Farrell, D. L., Weitz, O., Magnasco, M.O. & Zallen, J. A. (2017) SEGGA: a toolset for rapid automated analysis of epithelial cell polarity and dynamics. *Development* **144**, 1725–1734.

Fidorra, M., García, A., Ipsen, J. H., Härtel, S. & Bagatolli, L. A. (2009) Lipid domains in giant unilamellar vesicles and their correspondence with equilibrium thermodynamic phases: a quantitative fluorescence microscopy imaging approach. *Biochim. Biophys. Acta (BBA) – Biomembr.* **1788**, 2142–2149.

Fink, C., Morgan, F. & Loew, L. M. (1998) Intracellular fluorescent probe concentrations by confocal microscopy. *Biophys. J.* **75**, 1648–1658.

Frangi, A. F., Niessen, W. J., Vincken, K. L. & Viergever, M. A. (1998) Multiscale vessel enhancement filtering. In *Medical Image Computing and Computer-Assisted Intervention – MICCAI '98* (eds. W. M. Wells, A. Colchester and S. Delp), vol. **1496** of *Lecture Notes in Computer Science*, pp. 130–137. Springer, Berlin-Heidelberg.

Friedl, P. & Gilmour, D. (2009) Collective cell migration in morphogenesis, regeneration and cancer. *Nat. Rev. Mol. Cell Biol.* **10**, 445–457.

Härtel, S., Jara, J., Lemus, C. G. & Concha, M. L. (2007) 3D morphotopological analysis of asymmetric neuronal morphogenesis in developing zebrafish. In *Computational Modeling of Objects Represented in Images. Fundamentals, Methods and Applications* (eds. J. M. Tavares and J. Nata), pp. 215–220. Coimbra, Portugal, Taylor and Francis Group.

Kass, M., Witkin, A. & Terzopoulos, D. (1988) Snakes: active contour models. *Int. J. Comp. Vision* **1**, 321–331.

Kubitschek, U. (ed.) (2017) *Fluorescence Microscopy: From Principles to Biological Applications*, 2nd edn. Wiley-VCH, Weinheim, Germany.

Lecaudey, V., Cakan-Akdogan, G., Norton, W. H. J. & Gilmour, D. (2008) Dynamic Fgf signaling couples morphogenesis and migration in the zebrafish lateral line primordium. *Development* **135**, 2695–2705.

Luck BL, Carlson KD, Bovik AC, Richards-Kortum RR. (2005) An image model and segmentation algorithm for reflectance confocal images of in vivo cervical tissue. *IEEE Transact. Image Process.* **14**, 1265–1276.

Mashburn, D. N., Lynch H. E., Ma, X. & Hutson, M. S. (2012) Enabling user-guided segmentation and tracking of surface labeled cells in time-lapse image sets of living tissues. *Cytometry A* **85**, 409–418.

McInerney, T. & Terzopoulos, D. (1995) Topologically adaptable snakes. In *Proceedings of the Fifth International Conference on Computer Vision (ICCV'95)*, pp. 840–845.

Michelin, G., Guignard, L., Fiuza, U.-M. & Mandalain, G. (2014) Embryo cell membranes reconstruction by tensor voting. In *Proceedings of the IEEE 11th International Symposium on Biomedical Imaging (ISBI)*. Beijing, China. pp. 1259–1262.

Mosaliganti K, Gelas A, Gouaillard A, Noche R, Obholzer N, Megason S. (2009) Detection of spatially correlated objects in 3D images using appearance models and coupled active contours. *Med. Image Comput. Comp.-Assisted Interv.* **12**, 641–648.

Mosaliganti, K. R., Noche, R. R., Xiong, F., Swinburne, I. A. & Megason, S. G. (2012) ACME: automated cell morphology extractor for comprehensive reconstruction of cell membranes. *PLoS Comput. Biol.* **8**, e1002780.

Namías, R., D'Amato, J. P., del Fresno, M., Vénere, M., Pirró, N. & Bellemare, M.-E. (2016) Multi-object segmentation framework using deformable models for medical imaging analysis. *Med. Biol. Eng. Comput.* **54**, 1181–1192.

Osher, S. & Paragios, N. (2003) *Geometric Level Set Methods in Imaging, Vision, and Graphics*, 3rd edn. Springer-Verlag New York, Secaucus, NJ.

Pawley, J. (ed.) (2006) *Handbook of Biological Confocal Microscopy* (Chapter 3), 3rd edn. New York, US: Springer-Verlag.

Regan, J. C., Concha, M. L., Roussigne, M., Russell, C. & Wilson, S.W. (2009) An Fgf8-dependent bistable cell migratory event establishes CNS asymmetry. *Neuron* **61**, 27–34.

Reig, G., Cerda, M., Sepúlveda, N., Flores, D., Castañeda V., Tada, M., Härtel, S. & Concha, M. L. (2017) Extra-embryonic tissue spreading directs early embryo morphogenesis in killifish. *Nat. Commun.* **8**, 1–14.

Richardson, J., Gauert, A., Briones-Montecinos, L. *et al.* (2016) Leader cells define directionality of trunk, but not cranial, neural crest cell migration. *Cell Reports*, **15**, 2076–2088.

Rørth, P. (2009) Collective cell migration. *Ann. Rev. Cell Dev. Biol.* **25**, 407–429.

Roycroft, A. & Mayor, R. (2018) Michael Abercrombie: contact inhibition of locomotion and more. *Int. J. Dev. Biol.* **62**, 5–13.

Sanchez-Corrales, Y. E., Blanchard, G. B. & Röper, K. (2018) Radially patterned cell behaviours during tube budding from an epithelium. *eLife* **7**, e35717.

Sarder, P., & Nehorai, A. (2006). Deconvolution methods for 3-D fluorescence microscopy images. *IEEE Signal Process. Magaz.* **23**(3), 32–45.

Sarti, A., Malladi, R. & Sethian, J. A. (2002) Subjective surfaces: A geometric model for boundary completion. *Int. J. Comp. Vision* **46**, 201–221.

Stegmaier J, Amat F, Lemon WC, McDole K, Wan Y, Teodoro G, Mikut R, Keller PJ. (2005) Real-time three-dimensional cell segmentation in large-scale microscopy data of developing embryos. *Dev. cell* **336**, 225–240.

Stegmaier, J., Amat, F., Lemon, W. C., McDole, K., Wan, Y., Teodoro, G., Mikut, R. & Keller, P. J. (2016) Real-time three dimensional cell segmentation in large-scale microscopy data of developing embryos. *Dev. Cell* **36**, 225–240.

Sørensen, T. (1948) A method of establishing groups of equal amplitude in plant sociology based on similarity of species and its application to analyses of the vegetation on Danish commons. *Kong. Danske Vidensk. Selskab* **5**, 1–34.

Vachier, C. & Meyer, F. (2005) The viscous watershed transform. *J. Mathem. Imaging Vision* **22**, 251–267.

Veldhuis, J. H., Ehsandar, A., Maître, J.-L., Hiiragi, T., Cox, S. & Brodland, G. W. (2017) Inferring cellular forces from image stacks. *Philos. Transact. R. Soc. B: Biol. Sci.* **372**, 20160261.

Weiler, K. & Atherton, P. (1977) Hidden surface removal using polygon area sorting. *Comput. Graph.* **11**, 214–222.

Xu, C. & Prince, J. L. (1998a) Generalized gradient vector flow external forces for active contours. *Signal Process.* **71**, 131–139.

Xu, C. & Prince, J. L. (1998b) Snakes, shapes, and gradient vector flow. *IEEE Transact. Image Process.* **7**, 359–369.

Yap, A. S., Duszyc, K. & Viasnoff, V. (2018) Mechanosensing and mechanotransduction at cell–cell junctions. *Cold Spring Harbor Perspect. Biol.* **10**, a028761.

Yates, R. C. (1974) *Curves and Their Properties*. National Council of Teachers of Mathematics. Inc. 1906 Association Drive. Reston, Virginia 22091, USA.

Supporting Information

Additional supporting information may be found online in the Supporting Information section at the end of the article.

Fig. S1. Interexpert variations (Expert 1/2/3) of Manually Outlined Contours (MOCs, panels A/D/G), optimised Parametric Active Contours (PACs, panels B/E/H), and ALPACA (panels C/F/I) of 16 PpO cells from Fig. 1 .

Fig. S2. ALPACA correctly defines adjacent and nonadjacent sections from manually outlined object contours.

Table S1. Morphological indices for cell area and perimeter (A) and similarity indices (B) for three independent experts (E1/E2/E3) for $n = 51$ PpO cells.

Table S2. Morphological indices for cell area and perimeter (A) and similarity indices (B) for three independent experts (E1/E2/E3) against Ground Truth (GT) for $n = 88$ synthetic hexagonal cells.

Table S3. Morphological indices for cell area and perimeter (A) and similarity indices (B) for three independent experts (E1/E2/E3) for $n = 88$ synthetic hexagonal cells.